



저작자표시-비영리-변경금지 2.0 대한민국

이용자는 아래의 조건을 따르는 경우에 한하여 자유롭게

- 이 저작물을 복제, 배포, 전송, 전시, 공연 및 방송할 수 있습니다.

다음과 같은 조건을 따라야 합니다:



저작자표시. 귀하는 원저작자를 표시하여야 합니다.



비영리. 귀하는 이 저작물을 영리 목적으로 이용할 수 없습니다.



변경금지. 귀하는 이 저작물을 개작, 변형 또는 가공할 수 없습니다.

- 귀하는, 이 저작물의 재이용이나 배포의 경우, 이 저작물에 적용된 이용허락조건을 명확하게 나타내어야 합니다.
- 저작권자로부터 별도의 허가를 받으면 이러한 조건들은 적용되지 않습니다.

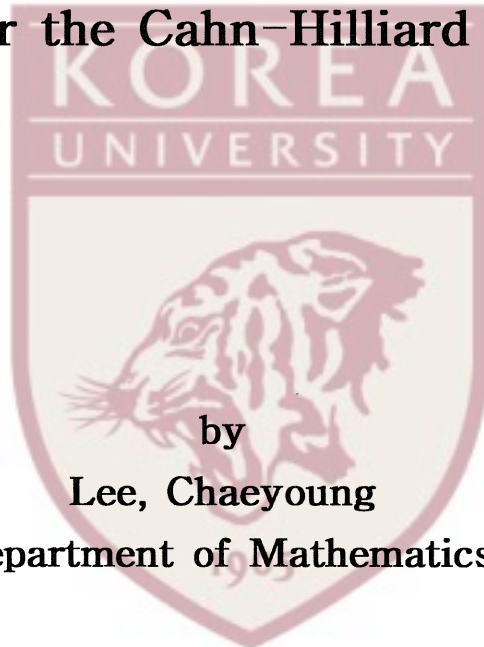
저작권법에 따른 이용자의 권리는 위의 내용에 의하여 영향을 받지 않습니다.

이것은 [이용허락규약\(Legal Code\)](#)을 이해하기 쉽게 요약한 것입니다.

[Disclaimer](#)

**Thesis for the Degree of Master**

**A fourth-order compact finite difference  
method for the Cahn-Hilliard equation**



**by**

**Lee, Chaeyoung**

**Department of Mathematics**

**Graduate School**

**Korea University**

**June, 2014**

김준석 教授指導  
碩士學位論文

**A fourth-order compact finite difference  
method for the Cahn-Hilliard equation**

이 論文을 理學碩士學位 論文으로 提出함.

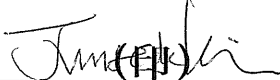
2014 年 6 月

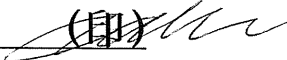
高麗大學校 大學院  
數學科  
李 宥 瑛




李宥瑛의 理學碩士學位 論文  
審査를 完了함.

2014 年 6 月 日

委員長 김 준 석  (印)

委員 안 인 경  (印)

委員 황 운 제  (印)



## Contents

List of Figures	iii
List of Tables	v
Acknowledgments	vi
Abstract	vii
Chapter 1. Introduction	1
Chapter 2. Fourth-order compact finite difference scheme	4
2.1. Numerical discretization	4
2.2. The Poisson equation	8
2.3. Heat equation	10
Chapter 3. Numerical method for the Cahn–Hilliard equation	12
3.1. Numerical solution	12
3.2. Mass conservation	14
3.3. Multigrid algorithm	15
Chapter 4. Numerical results for the Cahn–Hilliard equation	18

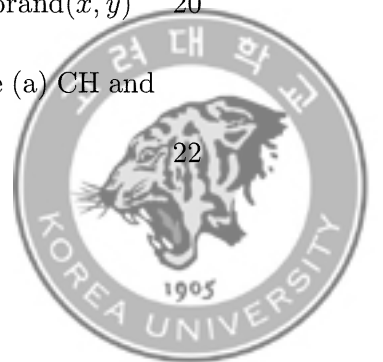


4.1. Convergence test	18
4.2. Non-increase of total energy and conservation of mass	20
4.3. Linear stability analysis	21
4.4. Stability of the proposed scheme	23
4.5. Steady state	24
4.6. Comparison of schemes	25
4.7. Comparison between CNPF and NPF	26
Chapter 5. Conclusion	27
Bibliography	28



## List of Figures

1.1	Free energy density $F(\phi)$	2
2.1	Discrete gradient of $\phi$ at a point ( $\blacklozenge$ ) is a combination of six circles ( $\bullet$ ).	5
2.2	Two-dimensional computational grids indicate (a) the five-point stencil, (b) the standard nine-point stencil, and (c) the compact nine-point stencil for the Laplacian operator at $(x_i, y_j)$ .	6
2.3	The exact solution of the Poisson equation.	9
2.4	(a) Initial condition $u(x, y, 0)$ and (b) exact solution $u^{ex}(x, y, T)$ at time $T = 0.025$ for heat equation.	11
4.1	(a) Initial condition $\phi(x, y, 0)$ and (b) numerical solution $\phi(x, y, T)$ at time $T = 0.0144$	19
4.2	Non-dimensional discrete total energy $\mathcal{E}^h(\phi^n)/\mathcal{E}^h(\phi^0)$ and mass concentration with the initial condition $\phi(x, y, 0) = 0.5\text{rand}(x, y)$	20
4.3	Growth rate versus the wave numbers $k_1$ and $k_2$ for the (a) CH and (b) linearized CH equations	22



4.4	Evolutions with different time step $\Delta t = 0.01, 10, \text{ and } 10000$	23
4.5	Evolution of $\phi$ up to the steady state time $t = 152.6$ . The times are shown below each figure.	24
4.6	Evolutions for FPF and CNPF with a mesh grid $256 \times 64$ . Note that the reference solution is defined by use much more finer mesh $1024 \times 256$ . From top to bottom, times are $t = 0, 2, 6, \text{ and } 10$ .	25
4.7	V-cycle number with different time step $\Delta t$	26





## List of Tables

2.1	$l_2$ -norm errors and convergence rates for FPF and CNPF	9
2.2	$l_2$ -norm errors and convergence rates for FPF and CNPF	11
4.1	$l_2$ -norm errors and convergence rates for FPF, NPF, and CNPF	19
4.2	CPU time (sec) for FPF, NPF, and CNPF	26



## Acknowledgments

I would like to express my gratitude to my advisor, Professor Junseok Kim for his support and for giving the opportunity to study at the laboratory. And I am thankful to other committee members of my thesis, Professor In Kyung Ahn and Woon Jae Hwang.

Also, I offer my regards and blessings to all of those who supported me for their help and assistance. I feel very glad to work with my research group.

Finally, my deepest gratitude goes to my family for their love and support.



## Abstract

A fourth-order accurate and practically stable compact finite difference method is proposed for the Cahn–Hilliard equation.

We present a compact finite difference stencil of the Laplacian operator in two-dimension. It is applied to the Poisson and heat equations and perform numerical experiments to verify their fourth-order accuracy. And, we present the compact scheme for the linearly stabilized splitting scheme for the Cahn–Hilliard equation. It is fourth-order accurate and practically stable. We solve the resulting system of discrete equations by a multigrid method. There are a variety of numerical experiments to show the fourth-order convergence, non-increase of total energy, mass conservation, linear stability analysis, robustness of the scheme, and evolution up to the steady state. Also, we demonstrate that the proposed scheme is more robust and efficient than the non-compact fourth-order scheme.

This thesis includes the contents in the following publication: “A fourth-order spatial accurate and practically stable compact scheme for the Cahn–Hilliard equation.” *Physica A: Statistical Mechanics and its Applications* 409 (2014) 17–28.



# Chapter 1

## Introduction

The Cahn–Hilliard equation was originally introduced as a phenomenological model of phase separation in a binary alloy [1, 2] and has been widely applied in many areas such as image processing [3, 4], microstructure [5], multi-phase fluid flows [6], planet formation [7], and tumor growth [8, 9]. The Cahn–Hilliard equation is

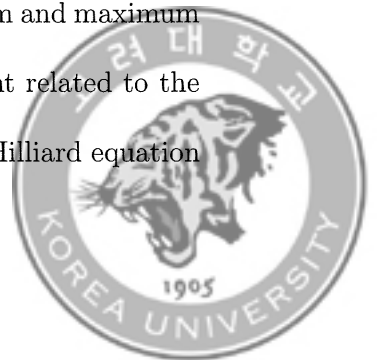
$$\frac{\partial\phi(\mathbf{x}, t)}{\partial t} = \nabla \cdot [M(\phi(\mathbf{x}, t))\nabla\mu(\phi(\mathbf{x}, t))], \quad \mathbf{x} \in \Omega, \quad t > 0, \quad (1.1)$$

$$\mu(\phi(\mathbf{x}, t)) = F'(\phi(\mathbf{x}, t)) - \epsilon^2\Delta\phi(\mathbf{x}, t), \quad (1.2)$$

where  $\Omega$  is a bounded domain that satisfies periodic boundary conditions for  $\phi$  and  $\mu$ . The quantity  $\phi(\mathbf{x}, t)$  is a phase-field order parameter, which is defined as the difference of mass concentrations of the components in a binary mixture.  $\mu$  is a chemical potential and  $M$  is a mobility. The free energy density

$$F(\phi) = \frac{1}{4}(\phi^2 - 1)^2$$

has a double-well potential that has two local minima at the minimum and maximum of the concentration as shown in Figure 1.1.  $\epsilon$  is a positive constant related to the interfacial thickness. The total free energy functional of the Cahn–Hilliard equation



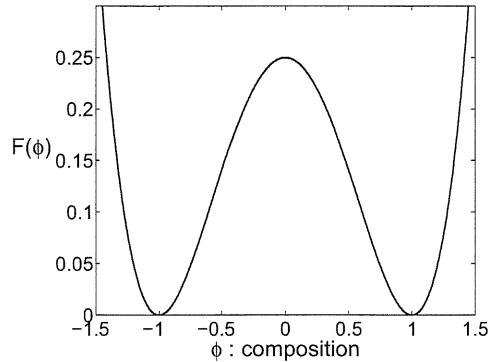


FIGURE 1.1. Free energy density  $F(\phi)$

is defined as

$$\mathcal{E}(\phi) = \int_{\Omega} \left( F(\phi) + \frac{\epsilon^2}{2} |\nabla \phi|^2 \right) dx.$$

We differentiate the energy  $\mathcal{E}(t)$  with respect to  $t$  and the total mass  $\int_{\Omega} \phi dx$  using the boundary condition,

$$\frac{d}{dt} \mathcal{E}(t) \leq 0 \quad \text{and} \quad \frac{d}{dt} \int_{\Omega} \phi dx = 0.$$

Therefore, the total energy is non-increasing in time  $t$  and the total mass is conserved.

The Cahn–Hilliard equation has fourth-order spatial derivatives and a Laplacian acting on the nonlinear term  $F'(\phi)$ . In general, explicit time discretizations require small time step sizes for stability. To overcome constraints of the time step sizes, several implicit time discretizations have been proposed [10, 11, 12, 13, 14, 15, 16]. However, most of these numerical solutions have the second-order accuracy in spatial discretizations. Note that the spectral [17, 18, 19] and finite element [20] methods for

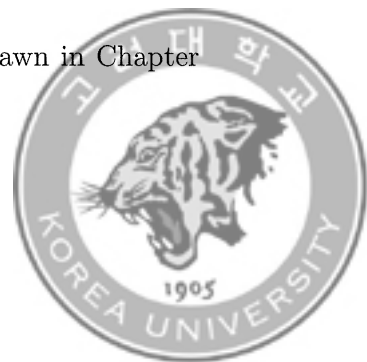


---

the Cahn–Hilliard equation can be approximated to arbitrary accuracy. However, there are advantages and disadvantages to each numerical method.

In recent years, high-order compact difference methods have been developed for simulating computational fluid dynamics [22], acoustics [23], electromagnetic [24, 25], and option pricing in stochastic volatility models [26]. Moreover, there are various studies about fourth-order compact schemes for the Poisson [27, 28, 29], heat [30], Navier–Stokes [31, 32, 33], biharmonic [34, 35], reaction-diffusion [36], and convection-diffusion [37, 38] equations. Also, sixth-order compact schemes for the Poisson [29, 39], Helmholtz [24], and convection-diffusion equations [22] have been developed. Up to now, there are many works on the second-order finite difference method but few works on the high-order difference method for the Cahn–Hilliard equation. Li *et al.* [40] established a three-level linearized compact difference scheme for the Cahn–Hilliard equation. In this thesis, we propose the compact scheme by combining a compact nine-point formula and linearly stabilized splitting scheme [41].

This thesis is organized as follows. In Chapter 2, we derive a fourth-order compact finite difference scheme. We consider the compact scheme for the Poisson and heat equations. In Chapter 3, the fourth-order accurate and practically stable compact scheme is presented for the Cahn–Hilliard equation. And, we describe the multigrid algorithm for the resulting system. In Chapter 4, there are various numerical experiments to demonstrate. Finally, conclusions are drawn in Chapter 5.



## Chapter 2

### Fourth-order compact finite difference scheme

#### 2.1. Numerical discretization

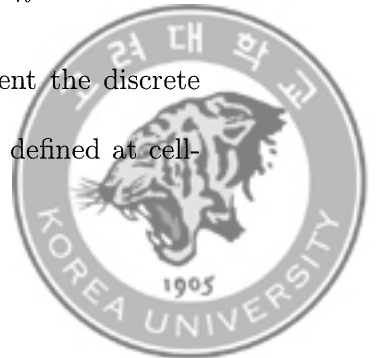
We consider discretizations in two-dimensional domain  $\Omega = (a, b) \times (c, d)$ . Let  $N_x$  and  $N_y$  be positive even integers,  $h = (b - a)/N_x = (d - c)/N_y$  be the uniform mesh size. We denote a discrete computational domain by  $\Omega_h = \{(x_i, y_j) : x_i = a + (i - 0.5)h, y_j = c + (j - 0.5)h, 1 \leq i \leq N_x, 1 \leq j \leq N_y\}$ , which is the set of cell-centers. Let  $\phi_{ij}^n$  be the approximation of  $\phi(x_i, y_j, n\Delta t)$ , where  $\Delta t = T/N_t$  is the time step,  $T$  is the final time, and  $N_t$  is the total number of time steps. We use periodic boundary conditions for  $\phi$  and  $\mu$  as follows:

$$\phi_{i0} = \phi_{i,N_x}, \phi_{i,N_x+1} = \phi_{i1}, \phi_{0j} = \phi_{N_y,j}, \phi_{N_y+1,j} = \phi_{1j}.$$

The discrete differentiation operators are

$$\begin{aligned} D_x \phi_{i+\frac{1}{2},j} &= \frac{1}{12} \frac{\phi_{i+1,j+1} - \phi_{i,j+1}}{h} + \frac{5}{6} \frac{\phi_{i+1,j} - \phi_{ij}}{h} + \frac{1}{12} \frac{\phi_{i+1,j-1} - \phi_{i,j-1}}{h}, \\ D_y \phi_{i,j+\frac{1}{2}} &= \frac{1}{12} \frac{\phi_{i+1,j+1} - \phi_{i+1,j}}{h} + \frac{5}{6} \frac{\phi_{i,j+1} - \phi_{ij}}{h} + \frac{1}{12} \frac{\phi_{i-1,j+1} - \phi_{i-1,j}}{h}, \end{aligned}$$

and we use the notation  $\nabla_c \phi_{ij} = \left( D_x \phi_{i+\frac{1}{2},j}, D_y \phi_{i,j+\frac{1}{2}} \right)$  to represent the discrete gradient of  $\phi$  (see Figure 2.1). The discrete divergence operator is defined at cell-



## 2.1. NUMERICAL DISCRETIZATION

---

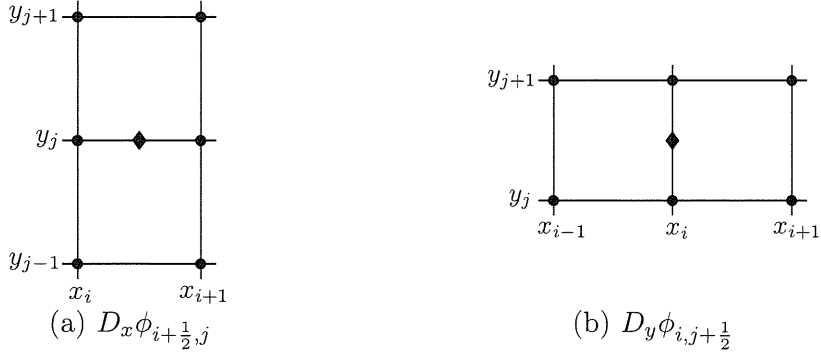


FIGURE 2.1. Discrete gradient of  $\phi$  at a point ( $\blacklozenge$ ) is a combination of six circles ( $\bullet$ ).

center point as

$$\nabla_d \cdot (u, v)_{ij} = \frac{u_{i+\frac{1}{2}, j} - u_{i-\frac{1}{2}, j}}{h} + \frac{v_{i, j+\frac{1}{2}} - v_{i, j-\frac{1}{2}}}{h}.$$

We then define the discrete  $l_2$ -inner products as

$$(\phi, \psi)_h := h^2 \sum_{i=1}^{N_x} \sum_{j=1}^{N_y} \phi_{ij} \psi_{ij},$$

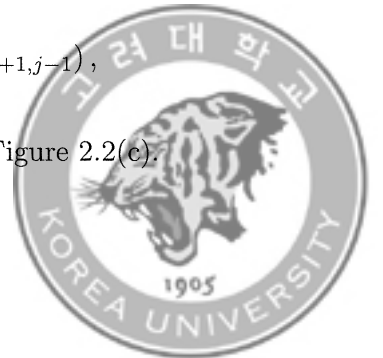
$$(\nabla_c \phi, \nabla_c \psi)_e := h^2 \sum_{i=1}^{N_x} \sum_{j=1}^{N_y} \left( D_x \phi_{i+\frac{1}{2}, j} D_x \psi_{i+\frac{1}{2}, j} + D_y \phi_{i, j+\frac{1}{2}} D_y \psi_{i, j+\frac{1}{2}} \right),$$

and the discrete norms as  $\|\phi\|^2 = (\phi, \phi)_h$  and  $\|\nabla \phi\|_e^2 = (\nabla_c \phi, \nabla_c \phi)_e$ .

The compact nine-point Laplacian operator  $\Delta_c$  [42] is defined as

$$\begin{aligned} \Delta_c \phi_{ij} &= \nabla_d \cdot \nabla_c \phi_{ij} \\ &= \frac{1}{6h^2} (\phi_{i-1, j+1} + 4\phi_{i, j+1} + \phi_{i+1, j+1} + 4\phi_{i-1, j} \\ &\quad - 20\phi_{ij} + 4\phi_{i+1, j} + \phi_{i-1, j-1} + 4\phi_{i, j-1} + \phi_{i+1, j-1}), \end{aligned} \tag{2.1}$$

and its stencil for the discrete Laplacian operator is illustrated in Figure 2.2(c).





## 2.1. NUMERICAL DISCRETIZATION

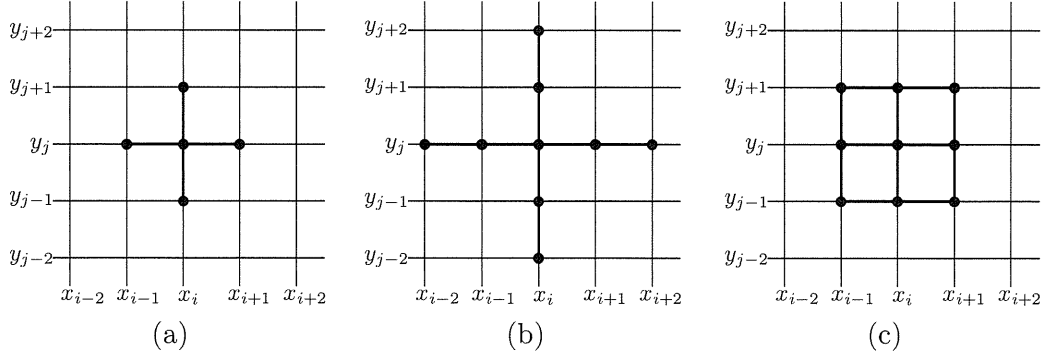


FIGURE 2.2. Two-dimensional computational grids indicate (a) the five-point stencil, (b) the standard nine-point stencil, and (c) the compact nine-point stencil for the Laplacian operator at  $(x_i, y_j)$ .

By using the Taylor series in two variables, we can obtain

$$\begin{aligned} \phi(x + \Delta x, y + \Delta y) &= \sum_{k=0}^5 \frac{1}{k!} \left( \Delta x \frac{\partial}{\partial x} + \Delta y \frac{\partial}{\partial y} \right)^k \phi(x, y) \\ &\quad + O((\Delta x)^6 + (\Delta y)^6). \end{aligned}$$

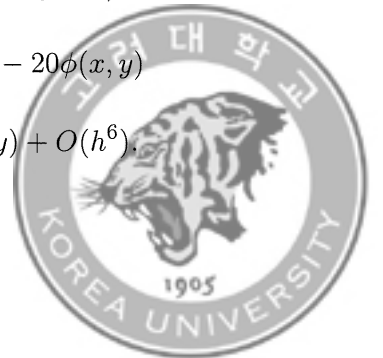
By replacing  $\Delta x$  and  $\Delta y$  with different values  $\pm h$ , we get

$$\begin{aligned} &\phi(x + h, y) + \phi(x - h, y) + \phi(x, y - h) + \phi(x, y + h) \\ &= 4\phi + h^2\phi_{xx} + h^2\phi_{yy} + \frac{h^4}{12}\phi_{xxxx} + \frac{h^4}{12}\phi_{yyyy} + O(h^6), \end{aligned} \quad (2.2)$$

$$\begin{aligned} &\phi(x - h, y - h) + \phi(x - h, y + h) + \phi(x + h, y - h) + \phi(x + h, y + h) \\ &= 4\phi + 2h^2\phi_{xx} + 2h^2\phi_{yy} + \frac{h^4}{6}\phi_{xxxx} + h^4\phi_{xxyy} + \frac{h^4}{6}\phi_{yyyy} + O(h^6). \end{aligned} \quad (2.3)$$

From Equations (2.2) and (2.3), we have

$$\begin{aligned} &\phi(x - h, y - h) + \phi(x - h, y + h) + \phi(x + h, y - h) + \phi(x + h, y + h) \\ &\quad + 4[\phi(x + h, y) + \phi(x - h, y) + \phi(x, y - h) + \phi(x, y + h)] - 20\phi(x, y) \\ &= 6h^2(\phi_{xx} + \phi_{yy})(x, y) + \frac{h^4}{2}(\phi_{xxxx} + 2\phi_{xxyy} + \phi_{yyyy})(x, y) + O(h^6). \end{aligned}$$



## 2.1. NUMERICAL DISCRETIZATION

---

Finally, we have

$$\Delta_c \phi_{ij} = \Delta \phi(x_i, y_j) + \frac{h^2}{12} \Delta^2 \phi(x_i, y_j) + O(h^4), \quad (2.4)$$

where  $\Delta^2 \phi = \Delta(\Delta \phi)$  is the biharmonic operator. For the sake of convenience, we call this approximation *compact nine-point formula* (CNPF).

Note that the standard fourth-order nine-point Laplacian operator  $\Delta_s$  is defined as

$$\begin{aligned} \Delta_s \phi_{ij} &= \frac{1}{12h^2} (-\phi_{i-2,j} + 16\phi_{i-1,j} - 30\phi_{ij} + 16\phi_{i+1,j} - \phi_{i+2,j}) \\ &\quad + \frac{1}{12h^2} (-\phi_{i,j-2} + 16\phi_{i,j-1} - 30\phi_{ij} + 16\phi_{i,j+1} - \phi_{i,j+2}), \end{aligned}$$

and its stencil is shown in Figure 2.2(b). In a similar manner, we can derive

$$\Delta_s \phi_{ij} = \Delta \phi(x_i, y_j) + O(h^4).$$

We call this approximation *nine-point formula* (NPF).

In Figure 2.2(a), a second-order five-point stencil is represented for the discrete Laplacian operator  $\Delta_d \phi_{ij} = (\phi_{i+1,j} + \phi_{i-1,j} + \phi_{i,j-1} + \phi_{i,j+1} - 4\phi_{ij})/h^2$ , and we define *five-point formula* (FPF) as

$$\Delta_d \phi_{ij} = \Delta \phi(x_i, y_j) + O(h^2).$$



### 2.2. The Poisson equation

We consider the two-dimensional Poisson equation with a periodic boundary condition,

$$\Delta u(x, y) = f(x, y), \quad (x, y) \in \Omega. \quad (2.5)$$

Now, applying CNPF (2.4) to Equation (2.5), we obtain

$$\begin{aligned} \Delta_c u_{ij} &= \Delta u + \frac{h^2}{12} \Delta^2 u + O(h^4) = f + \frac{h^2}{12} \Delta f + O(h^4) \\ &= f_{ij} + \frac{h^2}{12} (\Delta_c f_{ij} + O(h^2)) + O(h^4) \\ &= f_{ij} + \frac{h^2}{12} \Delta_c f_{ij} + O(h^4). \end{aligned} \quad (2.6)$$

Using Equations (2.1) and (2.6), the compact scheme for solving Equation (2.5) is

$$\begin{aligned} &\frac{1}{6h^2} [4(u_{i,j+1} + u_{i,j-1} + u_{i+1,j} + u_{i-1,j}) \\ &\quad + (u_{i+1,j+1} + u_{i+1,j-1} + u_{i-1,j+1} + u_{i-1,j-1}) - 20u_{ij}] \\ &= f_{ij} + \frac{1}{72} [4(f_{i,j+1} + f_{i,j-1} + f_{i+1,j} + f_{i-1,j}) \\ &\quad + (f_{i+1,j+1} + f_{i+1,j-1} + f_{i-1,j+1} + f_{i-1,j-1}) - 20f_{ij}]. \end{aligned} \quad (2.7)$$

For instance, we take  $f(x, y) = -8\pi^2 \cos(2\pi x) \cos(2\pi y)$  in the Poisson equation (2.5) and its domain is  $\Omega = (0, 1) \times (0, 1)$ . Then the exact solution for the equation is

$$u^{ex}(x, y) = \cos(2\pi x) \cos(2\pi y)$$

as shown in Figure 2.3.



## 2.2. THE POISSON EQUATION

---

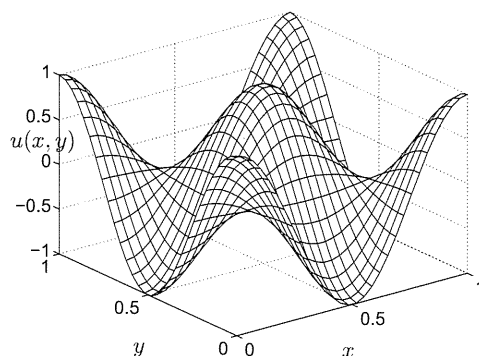


FIGURE 2.3. The exact solution of the Poisson equation.

We denote the error by  $e_{ij} := u_{ij} - u_{ij}^{ex}$ . The convergence rate is defined as the ratio of successive errors,  $\log_2(\|e_h\|/\|e_{h/2}\|)$ , where  $\|e_h\|$  is the discrete  $l_2$ -norm of error function  $e_h$ . The numerical convergence tests for Equation (2.7) using the three schemes are performed with increasingly finer grids  $h = 1/2^n$ , for  $n = 3, \dots, 8$ .

Table 2.1 lists the discrete  $l_2$ -norm of errors and convergence rates with three different formulas. Using CNPF, we have the fourth-order accuracy in space as we expect from the discretization.

TABLE 2.1.  $l_2$ -norm errors and convergence rates for FPF and CNPF

$h$	FPF		CNPF	
	error	order	error	order
1/8	$2.651 \times 10^{-2}$		$5.065 \times 10^{-4}$	
1/16	$6.475 \times 10^{-3}$	2.034	$3.272 \times 10^{-5}$	3.952
1/32	$1.609 \times 10^{-3}$	2.008	$2.060 \times 10^{-6}$	3.990
1/64	$4.018 \times 10^{-4}$	2.002	$1.289 \times 10^{-7}$	3.997
1/128	$1.004 \times 10^{-4}$	2.001	$8.063 \times 10^{-9}$	3.999
1/256	$2.510 \times 10^{-5}$	2.000	$5.069 \times 10^{-10}$	3.991



### 2.3. Heat equation

We consider the two-dimensional heat equation with a periodic boundary condition,

$$u_t(x, y, t) = \Delta u(x, y, t), \quad (x, y) \in \Omega, \quad 0 < t \leq T. \quad (2.8)$$

Now, applying CNPF (2.4) to Equation (2.8), we obtain

$$\begin{aligned} \Delta_c u_{ij} &= \Delta u + \frac{h^2}{12} \Delta^2 u + O(h^4) = u_t + \frac{h^2}{12} \Delta u_t + O(h^4) \\ &= u_t + \frac{h^2}{12} (\Delta_c u_t + O(h^2)) + O(h^4) \\ &= u_t + \frac{h^2}{12} \Delta_c u_t + O(h^4). \end{aligned} \quad (2.9)$$

We apply backward time difference to Equation (2.9), then

$$\Delta_c u_{ij}^{n+1} = \frac{u_{ij}^{n+1} - u_{ij}^n}{\Delta t} + \frac{h^2}{12} \frac{\Delta_c u_{ij}^{n+1} - \Delta_c u_{ij}^n}{\Delta t}.$$

By arranging the above equation, we get

$$\frac{1}{\Delta t} u_{ij}^{n+1} - \left(1 - \frac{h^2}{12\Delta t}\right) \Delta_c u_{ij}^{n+1} = \frac{1}{\Delta t} u_{ij}^n + \frac{h^2}{12\Delta t} \Delta_c u_{ij}^n. \quad (2.10)$$

For example, we use the initial condition for heat equation (2.8)

$$u(x, y, 0) = \cos(2\pi x) \cos(2\pi y),$$

in a domain  $\Omega = (0, 1) \times (0, 1)$  and the exact solution is

$$u^{ex}(x, y, t) = e^{-8\pi^2 t} \cos(2\pi x) \cos(2\pi y)$$

as shown in Figure 2.4.



## 2.3. HEAT EQUATION

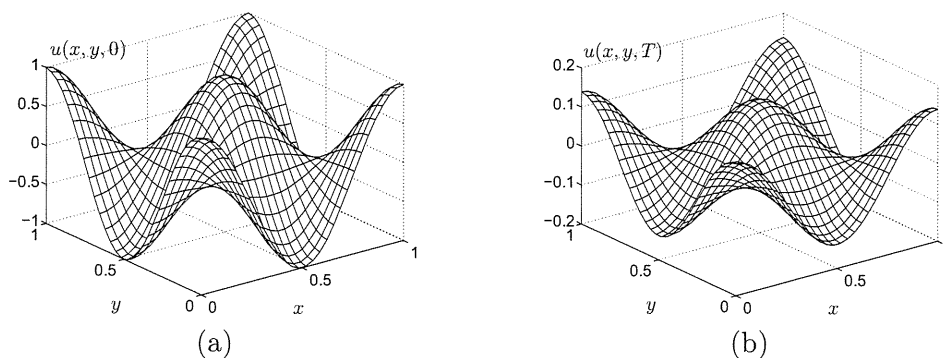


FIGURE 2.4. (a) Initial condition  $u(x, y, 0)$  and (b) exact solution  $u^{ex}(x, y, T)$  at time  $T = 0.025$  for heat equation.

We take convergence tests for Equation (2.10). Table 4.1 lists the discrete  $l_2$ -norm of errors and convergence rates with three different formulas. Using CNPF, we have the fourth-order accuracy in space as we expect from the discretization.

TABLE 2.2.  $l_2$ -norm errors and convergence rates for FPF and CNPF

h	FPF		CNPF	
	$L_2$ error	order	$L_2$ error	order
1/8	$1.988 \times 10^{-7}$		$1.676 \times 10^{-11}$	
1/16	$5.049 \times 10^{-8}$	1.977	$1.045 \times 10^{-12}$	4.003
1/32	$1.268 \times 10^{-8}$	1.993	$6.522 \times 10^{-14}$	4.002
1/64	$3.185 \times 10^{-9}$	1.993	$4.061 \times 10^{-15}$	4.005
1/128	$8.082 \times 10^{-10}$	1.979	$2.515 \times 10^{-16}$	4.013
1/256	$2.138 \times 10^{-10}$	1.919	$6.301 \times 10^{-17}$	1.997



# Chapter 3

## Numerical method for the Cahn–Hilliard equation

For the sake of convenience, the constant mobility is taken as  $M = 1$  throughout this thesis. Then the Cahn–Hilliard equation (1.1) and (1.2) is rewritten as

$$\frac{\partial \phi(\mathbf{x}, t)}{\partial t} = \Delta \mu(\phi(\mathbf{x}, t)), \quad (3.1)$$

$$\mu(\phi(\mathbf{x}, t)) = F'(\phi(\mathbf{x}, t)) - \epsilon^2 \Delta \phi(\mathbf{x}, t), \quad (3.2)$$

where  $\Omega \subset \mathbb{R}^2$  is a domain,  $\mathbf{x} = (x, y) \in \Omega$ ,  $t > 0$ .

### 3.1. Numerical solution

We derive the fourth-order accurate and practically stable compact finite difference scheme for the Cahn–Hilliard equation (3.1) and (3.2). Beginning with the compact nine-point Laplacian operator for  $\mu_{ij}$ , we have

$$\begin{aligned} \Delta_c \mu_{ij} &= \Delta \mu(x_i, y_j) + \frac{h^2}{12} \Delta^2 \mu(x_i, y_j) + O(h^4) \\ &= \phi_t(x_i, y_j) + \frac{h^2}{12} \Delta \phi_t(x_i, y_j) + O(h^4) \\ &= (\phi_t)_{ij} + \frac{h^2}{12} \Delta_c (\phi_t)_{ij} + O(h^4). \end{aligned} \quad (3.3)$$



### 3.1. NUMERICAL SOLUTION

---

Note that Equation (3.1) is used for the second equality in Equation (3.3). We approximate the temporal operator  $\phi_t$  to first-order accuracy by treating it implicitly:

$$\Delta_c \mu_{ij}^{n+1} = \frac{\phi_{ij}^{n+1} - \phi_{ij}^n}{\Delta t} + \frac{h^2}{12} \frac{\Delta_c \phi_{ij}^{n+1} - \Delta_c \phi_{ij}^n}{\Delta t} + O(\Delta t) + O(h^4). \quad (3.4)$$

We apply the linearly stabilized splitting scheme [41] to Equation (3.2):

$$\mu^{n+1} = (\phi^3 - 3\phi)^n + 2\phi^{n+1} - \epsilon^2 \Delta \phi^{n+1}. \quad (3.5)$$

By applying CNPF (2.4) to Equation (3.5), we get

$$\begin{aligned} \Delta_c \phi_{ij}^{n+1} &= \frac{(\phi^3 - 3\phi)_{ij}^n + 2\phi_{ij}^{n+1} - \mu_{ij}^{n+1}}{\epsilon^2} \\ &\quad + \frac{h^2}{12} \Delta \left( \frac{(\phi^3 - 3\phi)^n + 2\phi^{n+1} - \mu^{n+1}}{\epsilon^2} \right)_{ij} + O(h^4) \\ &= \frac{(\phi^3 - 3\phi)_{ij}^n + 2\phi_{ij}^{n+1} - \mu_{ij}^{n+1}}{\epsilon^2} \\ &\quad + \frac{h^2}{12\epsilon^2} \left( \Delta_c (\phi^3 - 3\phi)_{ij}^n + 2\Delta_c \phi_{ij}^{n+1} - \Delta_c \mu_{ij}^{n+1} \right) + O(h^4). \end{aligned} \quad (3.6)$$

Finally, from Equation (3.4) and Equation (3.6), we have the fourth-order accurate and practically stable compact finite difference scheme for the Cahn–Hilliard equation:

$$\frac{\phi_{ij}^{n+1}}{\Delta t} + \frac{h^2}{12\Delta t} \Delta_c \phi_{ij}^{n+1} - \Delta_c \mu_{ij}^{n+1} = \frac{\phi_{ij}^n}{\Delta t} + \frac{h^2}{12\Delta t} \Delta_c \phi_{ij}^n, \quad (3.7)$$

$$\begin{aligned} -\frac{2}{\epsilon^2} \phi_{ij}^{n+1} + \left( 1 - \frac{h^2}{6\epsilon^2} \right) \Delta_c \phi_{ij}^{n+1} + \frac{1}{\epsilon^2} \mu_{ij}^{n+1} + \frac{h^2}{12\epsilon^2} \Delta_c \mu_{ij}^{n+1} \\ = \frac{1}{\epsilon^2} (\phi^3 - 3\phi)_{ij}^n + \frac{h^2}{12\epsilon^2} \Delta_c (\phi^3 - 3\phi)_{ij}^n. \end{aligned} \quad (3.8)$$





### 3.2. Mass conservation

We verify that the compact scheme inherits the total mass conservation. Taking the inner product to Equation (3.7) with a constant grid function  $\mathbf{1}$ , we get

$$(\phi^{n+1}, \mathbf{1})_h + \frac{h^2}{12} (\Delta_c \phi^{n+1}, \mathbf{1})_h - \Delta t (\Delta_c \mu^{n+1}, \mathbf{1})_h = (\phi^{n+1}, \mathbf{1})_h + \frac{h^2}{12} (\Delta_c \phi^n, \mathbf{1})_h.$$

For  $(\Delta_c \phi^n, \mathbf{1})_h$ , we have

$$\begin{aligned} (\Delta_c \phi^n, \mathbf{1})_h &= h^2 \sum_{i=1}^{N_x} \sum_{j=1}^{N_y} \Delta_c \phi_{ij}^n \\ &= h^2 \sum_{i=1}^{N_x} \sum_{j=1}^{N_y} \left( \frac{D_x \phi_{i+\frac{1}{2},j}^n - D_x \phi_{i-\frac{1}{2},j}^n}{h} + \frac{D_x \phi_{i,j+\frac{1}{2}}^n - D_x \phi_{i,j-\frac{1}{2}}^n}{h} \right) \\ &= h \sum_{j=1}^{N_y} \left( D_x \phi_{N_x+\frac{1}{2},j}^n - D_x \phi_{\frac{1}{2},j}^n \right) + h \sum_{i=1}^{N_x} \left( D_x \phi_{i,N_y+\frac{1}{2}}^n - D_x \phi_{i,\frac{1}{2}}^n \right) = 0. \end{aligned}$$

Here, we have used the periodic boundary condition for  $\phi$ , and  $(\Delta_c \phi^{n+1}, \mathbf{1})_h = (\Delta_c \mu^n, \mathbf{1})_h = 0$  can be proved in a similar manner. Thus, we have the mass conserving property, i.e.,  $(\phi^n, \mathbf{1})_h = (\phi^{n+1}, \mathbf{1})_h$ .



### 3.3. Multigrid algorithm

We briefly describe the multigrid method and implementation to solve the resulting system. We represent the discrete Cahn–Hilliard system as

$$L_h(\phi^{n+1}, \mu^{n+1}) = (\xi^n, \psi^n),$$

where the linear operator  $L_h$  is defined as

$$L_h(\phi^{n+1}, \mu^{n+1}) = \left( \frac{\phi_{ij}^{n+1}}{\Delta t} + \frac{h^2}{12\Delta t} \Delta_c \phi_{ij}^{n+1} - \Delta_c \mu_{ij}^{n+1}, \right. \\ \left. - \frac{2}{\epsilon^2} \phi_{ij}^{n+1} + \left(1 - \frac{h^2}{6\epsilon^2}\right) \Delta_c \phi_{ij}^{n+1} + \frac{1}{\epsilon^2} \mu_{ij}^{n+1} + \frac{h^2}{12\epsilon^2} \Delta_c \mu_{ij}^{n+1} \right),$$

and the source term is

$$(\xi^n, \psi^n) = \left( \frac{\phi_{ij}^n}{\Delta t} + \frac{h^2}{12\Delta t} \Delta_c \phi_{ij}^n, \frac{1}{\epsilon^2} (\phi^3 - 3\phi)_{ij}^n + \frac{h^2}{12\epsilon^2} \Delta_c (\phi^3 - 3\phi)_{ij}^n \right).$$

**3.3.1. Smoothing.** Compute  $(\bar{\phi}_k, \bar{\mu}_k)$  by applying  $\nu$  smoothing procedures to  $(\phi_k, \mu_k)$ .

$$(\bar{\phi}_k, \bar{\mu}_k) = \text{SMOOTH}^\nu(\phi_k, \mu_k, L_h, \xi_k, \psi_k)$$

on a mesh grid  $\Omega_k$ . The  $\text{SMOOTH}^\nu$  function means that it performs a SMOOTH relaxation operator with approximations  $\phi_k$  and  $\mu_k$ , and source terms  $\xi_k$  and  $\psi_k$ . The superscript  $\nu$  denotes how many times the given relaxation operator is applied to obtain the updated approximations  $(\bar{\phi}_k, \bar{\mu}_k)$ . This relaxation step is evaluated using pointwise Gauss–Seidal iterative methods. One SMOOTH relaxation operator step is completed by solving the system by a  $2 \times 2$  matrix inversion for each  $i$  and  $j$ .



**3.3.2. V-cycle.** One V-cycle step comprises the presmoothing, coarse grid correction, and postsmoothing steps. Please refer to the reference text for additional details and background [13].

$$\left(\phi_k^{n+1,m+1}, \mu_k^{n+1,m+1}\right) = \text{V-cycle}(k, \phi_k^{n+1,m}, \mu_k^{n+1,m}, L_h, \xi_k^n, \psi_k^n, \nu_1, \nu_2)$$

where  $\phi_k^{n+1,m+1}$  and  $\phi_k^{n+1,m}$  are the approximations of  $\phi_k^{n+1}$  before and after the V-cycle. Next, we define the V-cycle.

**Presmoothing**

$$\left(\bar{\phi}_k^{n+1,m}, \bar{\mu}_k^{n+1,m}\right) = \text{SMOOTH}^{\nu_1}(\phi_k^{n+1,m}, \mu_k^{n+1,m}, L_h, \xi_k^n, \psi_k^n).$$

**Coarse grid correction**

- 1) Find the defect:  $\left(\bar{d}_{1,k}^m, \bar{d}_{2,k}^m\right) = (\xi_k^n, \psi_k^n) - L_h \left(\bar{\phi}_k^{n+1,m}, \bar{\mu}_k^{n+1,m}\right)$ .
- 2) Restrict the defect:  $\bar{d}_{1,k-1}^m = I_k^{k-1} \bar{d}_{1,k}^m$ ,  $\bar{d}_{2,k-1}^m = I_k^{k-1} \bar{d}_{2,k}^m$ .
- 3) Evaluate approximations  $\left(\hat{v}_{1,k-1}^{n+1,m}, \hat{v}_{2,k-1}^{n+1,m}\right)$  of the following coarse grid system on  $\Omega_{k-1}$ :  $L_{2h} \left(\hat{v}_{1,k-1}^{n+1,m}, \hat{v}_{2,k-1}^{n+1,m}\right) = \left(\bar{d}_{1,k-1}^m, \bar{d}_{2,k-1}^m\right)$ . If  $k > 1$ , then we can solve the coarse the grid system using the zero grid functions as initial approximations and the defect functions as source terms

$$\left(\hat{v}_{1,k-1}^{n+1,m}, \hat{v}_{2,k-1}^{n+1,m}\right) = \text{V-cycle}(k-1, 0, 0, L_{2h}, \bar{d}_{1,k-1}^m, \bar{d}_{2,k-1}^m, \nu_1, \nu_2).$$

Otherwise, we apply the smoothing procedure to obtain the approximations.

- 4) Interpolate the correction:  $\hat{v}_{1,k}^{n+1} = I_{k-1}^k \hat{v}_{1,k-1}^{n+1,m}$ ,  $\hat{v}_{2,k}^{n+1} = I_{k-1}^k \hat{v}_{2,k-1}^{n+1,m}$ .



### 3.3. MULTIGRID ALGORITHM

---

5) Compute the corrected approximation on  $\Omega_k$ :

$$\left(\tilde{\phi}_k^{n+1,m}, \tilde{\mu}_k^{n+1,m}\right) = \left(\bar{\phi}_k^{n+1,m}, \bar{\mu}_k^{n+1,m}\right) + \left(\hat{v}_{1,k}^{n+1,m}, \hat{v}_{2,k}^{n+1,m}\right).$$

**Postsmoothing**

$$\left(\phi_k^{n+1,m+1}, \mu_k^{n+1,m+1}\right) = \text{SMOOTH}^{\nu_2} \left(\tilde{\phi}_k^{n+1,m}, \tilde{\mu}_k^{n+1,m}, L_h: \xi_k^n, \psi_k^n\right).$$

This completes the description of the V-cycle.



# Chapter 4

## Numerical results for the Cahn–Hilliard equation

Various numerical experiments are given to demonstrate the fourth-order convergence, non-increase of total energy, mass conservation, linear stability analysis, robustness of the scheme, and evolution up to the steady state. In addition, it is performed to verify that the compact scheme is more robust and efficient than the non-compact fourth-order scheme.

### 4.1. Convergence test

A numerical convergence test for the three schemes is performed with increasingly finer grids  $h = 1/2^n$ , for  $n = 3, 4, 5$ , and 6. The initial state is defined as  $\phi(x, y, 0) = 0.1 \cos(2\pi x) \cos(2\pi y)$  in  $\Omega = (0, 1) \times (0, 1)$  (Figure 4.1(a)), and Figure 4.1(b) illustrates the numerical solution at  $T = 24\Delta t$ , where we use  $\epsilon = 0.0075$  and  $\Delta t = 6 \times 10^{-4}$ . We consider a reference solution, because it is generally hard to find the exact solution of the Cahn–Hilliard equation. We define the reference solution  $\phi_{ij}^{ref}$  by the local average of numerical solution on a much finer grid, and then denote the error by  $e_{ij} := \phi_{ij} - \phi_{ij}^{ref}$ . We use a  $1024 \times 1024$  mesh grid and FPF for the



#### 4.1. CONVERGENCE TEST

---

reference solution  $\phi_{ij}^{ref}$ . The convergence rate is defined as the ratio of successive errors,  $\log_2(\|e_h\|/\|e_{h/2}\|)$ , where  $\|e_h\|$  is the discrete  $l_2$ -norm of error function  $e_h$ .

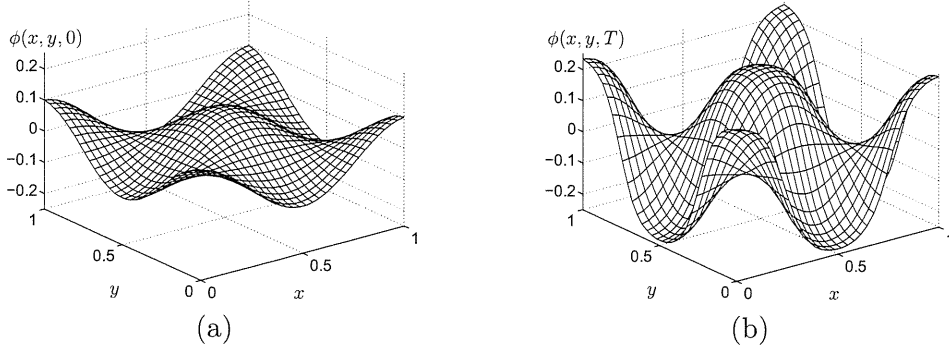


FIGURE 4.1. (a) Initial condition  $\phi(x, y, 0)$  and (b) numerical solution  $\phi(x, y, T)$  at time  $T = 0.0144$

Table 4.1 lists the discrete  $l_2$ -norm of errors and convergence rates with different three formula. Using NPF and CNPF, we have the fourth-order accuracy in space as we expect from the discretization.

TABLE 4.1.  $l_2$ -norm errors and convergence rates for FPF, NPF, and CNPF

$h$	FPF		NPF		CNPF	
	error	order	error	order	error	order
1/8	$1.03 \times 10^{-2}$		$8.14 \times 10^{-3}$		$5.02 \times 10^{-3}$	
1/16	$2.76 \times 10^{-3}$	1.90	$6.59 \times 10^{-4}$	3.63	$3.36 \times 10^{-4}$	3.90
1/32	$7.26 \times 10^{-4}$	1.93	$4.54 \times 10^{-5}$	3.86	$2.01 \times 10^{-5}$	4.06
1/64	$1.83 \times 10^{-4}$	1.99	$2.31 \times 10^{-6}$	4.30	$1.27 \times 10^{-6}$	3.98



## 4.2. Non-increase of total energy and conservation of mass

We define the discrete total energy functional by

$$\mathcal{E}^h(\phi^n) = (F(\phi^n), 1)_h + \frac{\epsilon^2}{2} \|\nabla \phi^n\|_e^2.$$

Figure 4.2 demonstrates that the discrete total energy is monotonically decreasing and the mass is conserved. The inscribed small figures show the phase separation at the indicated times. For the numerical test, in  $\Omega = (0, 1) \times (0, 1)$ , the initial state is taken as a random perturbation  $\phi(x, y, 0) = 0.5\text{rand}(x, y)$ , where  $\text{rand}(x, y)$  is a random value, which is uniformly distributed between  $-1$  and  $1$ . For other parameter,  $h = 1/256$ ,  $\Delta t = 0.002$ ,  $T = 3$ , and  $\epsilon = 0.0038$  are used.

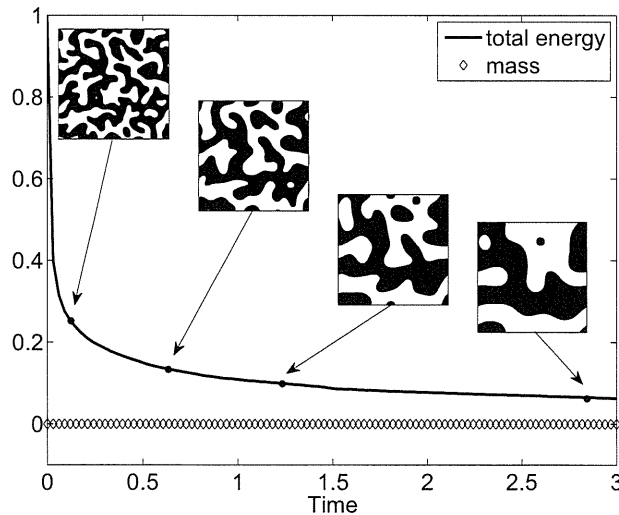
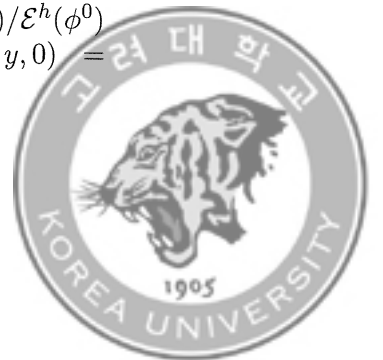


FIGURE 4.2. Non-dimensional discrete total energy  $\mathcal{E}^h(\phi^n)/\mathcal{E}^h(\phi^0)$  and mass concentration with the initial condition  $\phi(x, y, 0) = 0.5\text{rand}(x, y)$



### 4.3. Linear stability analysis

Let us consider the linear stability analysis for the Cahn–Hilliard equation (1.1) and (1.2)

$$\phi_t = \Delta (\phi^3 - \phi - \epsilon^2 \Delta \phi), \quad \mathbf{x} \in \Omega, \quad t > 0, \quad (4.1)$$

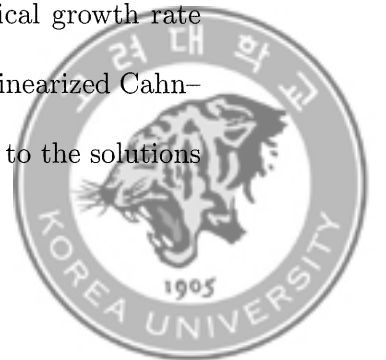
where  $\Omega = (0, 2\pi) \times (0, 2\pi)$ . We assume that the solution can be expressed by

$$\begin{aligned} \phi(x, y, t) = & \bar{\phi} + \sum_{k_1=1}^{\infty} \sum_{k_2=1}^{\infty} \beta_{k_1 k_2}(t) \cos(k_1 x) \cos(k_2 y) \\ & + \sum_{k_1=1}^{\infty} \sum_{k_2=1}^{\infty} \gamma_{k_1 k_2}(t) \sin(k_1 x) \sin(k_2 y), \end{aligned} \quad (4.2)$$

where  $\bar{\phi}$  is the average of  $\phi$ , and  $\beta_{k_1 k_2}(t)$  and  $\gamma_{k_1 k_2}(t)$  are amplification factors at wave numbers  $k_1$  and  $k_2$ . After linearizing Equation (4.1) and substituting Equation (4.2) into the linearized equation, we have

$$\frac{d\beta_{k_1 k_2}(t)}{dt} = k^2 (1 - 3\bar{\phi}^2 - \epsilon^2 k^2) \beta_{k_1 k_2}(t), \quad (4.3)$$

where we denote  $k^2 = k_1^2 + k_2^2$ . We only consider  $\beta_{k_1 k_2}(t)$  because the same ordinary differential equation holds for  $\gamma_{k_1 k_2}(t)$ . The solution of Equation (4.3) is  $\beta_{k_1 k_2}(t) = \beta_{k_1 k_2}(0) \exp(\eta_{k_1 k_2} t)$ , where  $\eta_{k_1 k_2} = k^2(1 - 3\bar{\phi}^2 - \epsilon^2 k^2)$  is the growth rate. The numerical growth rate is defined as  $\tilde{\eta}_{k_1 k_2} = \log(\|\phi^m\|_{\infty} / \|\phi^0\|_{\infty}) / (m\Delta t)$ . We take the initial condition  $\phi(x, y, 0) = 0.01 \cos(k_1 x) \cos(k_2 y)$  with  $m = 100$ ,  $\Delta t = 10^{-8}$ ,  $h = \pi/256$ , and  $\epsilon = 0.03$ . Figures 4.3(a) and (b) show the numerical growth rate  $\tilde{\eta}_{k_1 k_2}$  versus the wave numbers  $k_1$  and  $k_2$  for the Cahn–Hilliard and linearized Cahn–Hilliard equations, respectively. Open and closed circles correspond to the solutions





### 4.3. LINEAR STABILITY ANALYSIS

---

from the linear stability analysis and CNPF, respectively. The numerical results are in good agreement with the analytic solutions from the linear stability analysis.

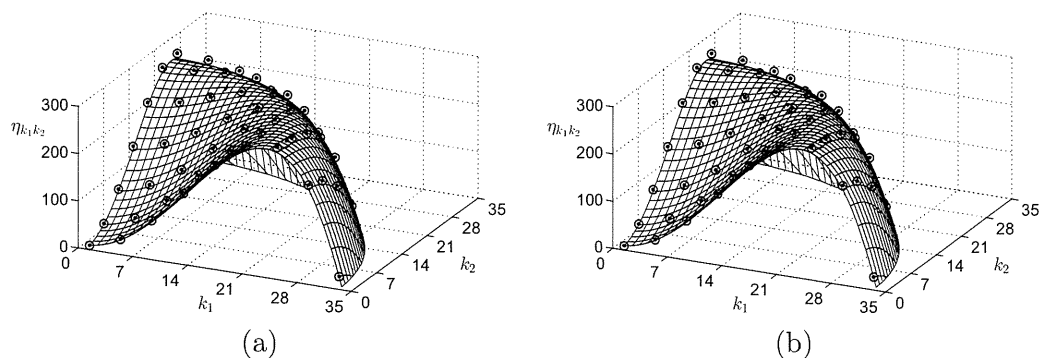
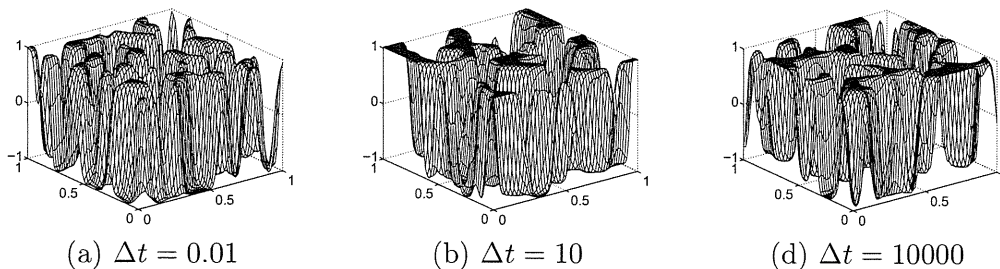


FIGURE 4.3. Growth rate versus the wave numbers  $k_1$  and  $k_2$  for the (a) CH and (b) linearized CH equations



## 4.4. Stability of the proposed scheme

We demonstrate a practical stability of the scheme through a numerical experiment with spinodal decomposition of a binary mixture. In the simulation, the initial condition is taken as  $\phi(x, y, 0) = 0.5\text{rand}(x, y)$  in  $\Omega = (0, 1) \times (0, 1)$ . Note that the maximum amplitude is 0.5 at the initial time. For numerical parameters,  $h = 1/128$  and  $\epsilon = 0.0113$  are used and different time step  $\Delta t = 0.01, 10, \text{ and } 10000$  are employed. In Figure 4.4, we illustrate the evolutions after fifteen time iterations. As the numerical results, the maximum amplitudes are bounded, and the numerical solutions do not blow up. Therefore, our proposed scheme is stable regardless of the time step size.

FIGURE 4.4. Evolutions with different time step  $\Delta t = 0.01, 10, \text{ and } 10000$ 

### 4.5. Steady state

We examine the evolution of a random perturbation up to the steady state. The initial condition is taken to be  $\phi(x, y, 0) = 0.01\text{rand}(x, y)$  in  $\Omega = (0, 1) \times (0, 1)$ . We then take the simulation parameters as  $\epsilon = 0.0075$ ,  $h = 1/256$ , and  $\Delta t = 10h^2$ . We stop the numerical computations when the discrete  $l_2$ -norm of the difference between  $(n + 1)$ th and  $n$ th step solutions becomes less than  $10^{-9}$ , i.e.,  $\|\phi^{n+1} - \phi^n\| \leq 10^{-9}$ . Figure 4.5 shows the snapshots of filled contour of the concentration  $\phi$ . We observe that the randomly perturbed concentration  $\phi$  evolves to a complex interconnected pattern. After a long time evolution, a numerical equilibrium state is reached.

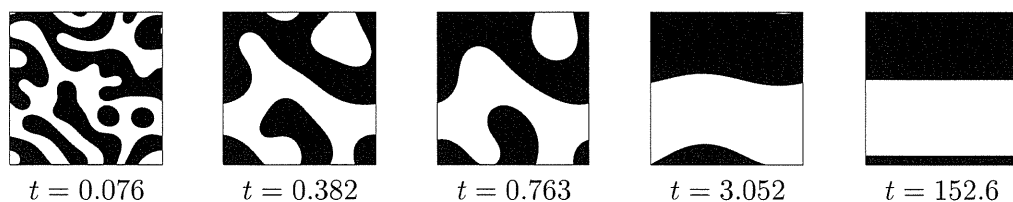


FIGURE 4.5. Evolution of  $\phi$  up to the steady state time  $t = 152.6$ . The times are shown below each figure.



## 4.6. Comparison of schemes

To show the superiority of CNPF, we compare the evolution results from CNPF and FPF, and list the computational times for the three methods. The initial condition is given as

$$\phi(x, y, 0) = \begin{cases} 1 & \text{if } 0.2 < x < 3.8 \text{ and } 0.4 < y < 0.6, \\ -1 & \text{otherwise} \end{cases} \quad (4.4)$$

in  $\Omega = (0, 4) \times (0, 1)$ . Here, a mesh grid  $256 \times 64$ ,  $\epsilon = 0.015$ ,  $\Delta t = 0.0005$ , and  $T = 10$  are used. We define the reference solution by numerical solutions, using FPF, on a finer mesh  $1024 \times 256$ . In Figure 4.6, we illustrate evolutions by CNPF (circles) and FPF (dashed line) with the reference solutions (solid line) at  $t = 0, 2, 6$ , and 10. Table 4.2 lists CPU times of the three schemes to  $T = 10$ . Although CNPF has a slight difference of CPU time than FPF, it has higher accuracy compared to FPF. Furthermore, NPF needs more V-cycle iterations than CNPF to reach the V-cycle tolerance, and it results in the increment of CPU time.

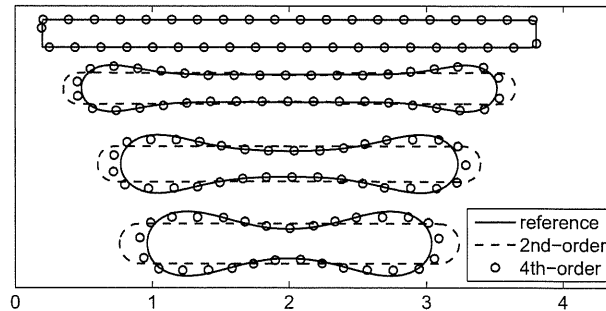


FIGURE 4.6. Evolutions for FPF and CNPF with a mesh grid  $256 \times 64$ . Note that the reference solution is defined by use much more finer mesh  $1024 \times 256$ . From top to bottom, times are  $t = 0, 2, 6$ , and 10.



#### 4.7. COMPARISON BETWEEN CNPF AND NPF

---

TABLE 4.2. CPU time (sec) for FPF, NPF, and CNPF

FPF	NPF	CNPF
1819	3095	2218

#### 4.7. Comparison between CNPF and NPF

We compare the numerical convergence of two formula, CNPF and NPF. For the numerical test, we take the initial condition as  $\phi(x, y, 0) = 0.1 \cos(2\pi x) \cos(2\pi y)$  in  $\Omega = (0, 1) \times (0, 1)$ . For other parameter, we use  $h = 1/64$  and  $\epsilon = 0.015$ . We count the number of V-cycle until the maximum value of residual error is less than  $10^{-10}$ . Figure 4.7 plots the numbers of V-cycle for one time iteration versus  $\Delta t$ . From the results, we can observe that CNPF requires less V-cycle iterations than NPF for all time step sizes.

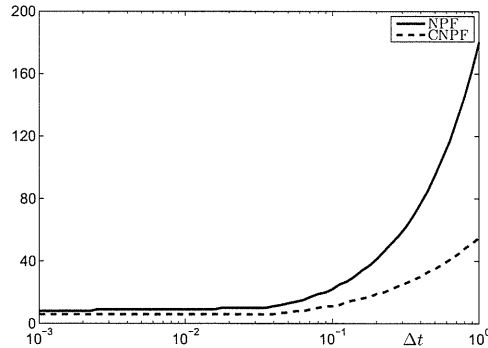


FIGURE 4.7. V-cycle number with different time step  $\Delta t$



# Chapter 5

## Conclusion

We proposed the fourth-order accurate and practically stable compact finite difference method for the Cahn–Hilliard equation. The compact nine-point formula (CNPF) and linearly stabilized splitting scheme were presented for the equation. We described the multigrid algorithm to solve the discrete Cahn–Hilliard system.

Numerical experiments were performed to demonstrate the fourth-order accuracy, decreasing of total energy, mass conservation, and practical stability. Also, to verify the superiority of proposed scheme, we compared the standard nine-point formula (NPF) with CNPF. Since NPF needs more V-cycle iterations than CNPF to reach the tolerance, the computational time of CNPF was less than that of NPF. NPF had a disadvantage due to the wide stencil compared to CNPF.

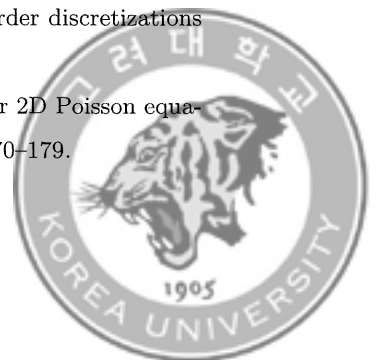


## Bibliography

- [1] J.W. Cahn, J.E. Hilliard, Free energy of a non-uniform system I. Interfacial free energy, *J. Chem. Phys.*, 28 (1958) 258–267.
- [2] J.W. Cahn, Free energy of a nonuniform system II: Thermodynamic basis, *J. Chem. Phys.*, 30 (1959) 1121–1124.
- [3] I.C. Dolcetta, S.F. Vita, R. March, Area-preserving curve-shortening flows: From phase separation to image processing, *Interfaces Free Boundaries*, 4 (2002) 325–343.
- [4] A.L. Bertozzi, S. Esedoglu, A. Gillette, Inpainting of binary images using the Cahn–Hilliard equation, *IEEE Trans. Image Process.*, 16 (2007) 285–291.
- [5] L.Q. Chen, Phase-field models for microstructure evolution, *Ann. Rev. Mater. Res.*, 32 (2002) 113–140.
- [6] J. Kim, A continuous surface tension force formulation for diffuse-interface models, *J. Comput. Phys.*, 204 (2005) 784–804.
- [7] S. Tremaine, On the origin of irregular structure in Saturn’s rings, *Astron. J.*, 125 (2003) 894–901.
- [8] S. Wise, J. Lowengrub, H. Frieboes, V. Cristini, Three-dimensional multispecies nonlinear tumor growth: I. Model and numerical method, *J. Theor. Biol.*, 253 (2008) 524–543.
- [9] V. Cristini, X. Li, J.S. Lowengrub, S.M. Wise, Nonlinear simulations of solid tumor growth using a mixture model: invasion and branching, *J. Math. Biol.*, 58 (2009) 723–763.
- [10] C.M. Elliott, The Cahn–Hilliard model for the kinetics of phase separation, in: J.F. Rodrigues (Ed.), *Mathematical models for phase change problems*, International Series of Numerical Mathematics 88, Birkhauser-Verlag, Basel (1989) 35–73.
- [11] M. Copetti, C.M. Elliott, Kinetics of phase decomposition processes: numerical solutions to the Cahn–Hilliard equation, *Labour Hist. Rev.*, 6 (1990) 273–283.
- [12] D. Furihata, A stable and conservative finite difference scheme for the Cahn–Hilliard equation, *Numer. Math.*, 87 (2001) 675–699.

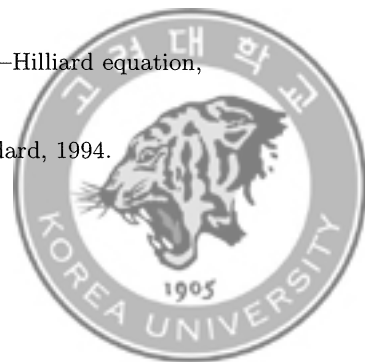


- 
- [13] J. Kim, K. Kang, J. Lowengrub, Conservative multigrid methods for Cahn–Hilliard fluids, *J. Comput. Phys.*, 193 (2004) 511–543.
- [14] E.V.L. de Mello, O.T. da S. Filho, Numerical study of the Cahn–Hilliard equation in one, two and three dimensions, *Physica A*, 347 (2005) 429–443.
- [15] H.G. Lee, J. Kim, A second-order accurate non-linear difference scheme for the N-component Cahn–Hilliard system, *Physica A*, 387 (2008) 4787–4799.
- [16] H.G. Lee, J.-W. Choi, J. Kim, A practically unconditionally gradient stable scheme for the N-component Cahn–Hilliard system, *Physica A*, 391 (2012) 1009–1019.
- [17] L. Chen, J. Shen, Applications of semi-implicit Fourier-spectral method to phase field equations, *Comput. Phys. Commun.*, 108 (1998) 147–158.
- [18] J. Zhu, L.Q. Chen, J. Shen, V. Tikare, Coarsening kinetics from a variable-mobility Cahn–Hilliard equation: application of a semi-implicit Fourier spectral method, *Phys. Rev. E*, 60 (1999) 3564–3572.
- [19] V.E. Badalassi, H.D. Ceniceros, S. Banerjee, Computation of multiphase systems with phase field models, *J. Comput. Phys.*, 190 (2003) 371–397.
- [20] D. Kay, R. Welford, A multigrid finite element solver for the Cahn–Hilliard equation. *J. Comput. Phys.*, 212 (2006) 288–304.
- [21] D.F. Martin, P. Colella, M. Anghel, F.L. Alexander, Adaptive mesh refinement for multiscale nonequilibrium physics, *Comput. Sci. Eng.*, 7 (2005) 24–31.
- [22] Y. Wang, J. Zhang, Fast and robust sixth-order multigrid computation for the three-dimensional convection-diffusion equation, *J. Comput. Appl. Math.*, 234 (2010) 3496–3506.
- [23] S. Kim, Compact schemes for acoustics in the frequency domain, *Math. Comput. Model.*, 37 (2003) 1335–1341.
- [24] E. Turkel, D. Gordon, R. Gordon, S. Tsynkov, Compact 2D and 3D sixth order schemes for the Helmholtz equation with variable wave number, *J. Comput. Phys.*, 232 (2013) 272–287.
- [25] J. Nordstrom, R. Gustafsson, High order finite difference approximations of electromagnetic wave propagation close to material discontinuities, *J. Sci. Comput.*, 18 (2003) 215–234.
- [26] B. Düring, M. Fournié, High-order compact finite difference scheme for option pricing in stochastic volatility models, *J. Comput. Appl. Math.*, 236 (2012) 4462–4473.
- [27] M.M. Gupta, J. Kouatchou, J. Zhang, Comparison of second and fourth order discretizations for multigrid Poisson solver, *J. Comput. Phys.*, 132 (1997) 226–232.
- [28] J. Zhang, Multigrid method and fourth order compact difference scheme for 2D Poisson equation with unequal meshsize discretization, *J. Comput. Phys.*, 179 (2002) 170–179.





- 
- [29] S. Zhai, X. Feng, Y. He, A family of fourth-order and sixth-order compact difference schemes for the three-dimensional Poisson equation, *J. Sci. Comput.*, 54 (2013) 97–120.
- [30] H. Sun, J. Zhang, A high-order compact boundary value method for solving one-dimensional heat equations, *Numer. Meth. Part Differ. Equ.*, 19 (2003) 846–857.
- [31] M. Li, T. Tang, A compact fourth-order finite difference scheme for unsteady viscous incompressible flows, *J. Sci. Comput.*, 16 (2001) 29–45.
- [32] W.F. Spitz, G.F. Carey, High-order compact scheme for the steady stream-function vorticity equations, *Int. J. Numer. Methods Eng.*, 38 (1995) 3497–3512.
- [33] M. Li, T. Tang, B. Fornberg, A compact fourth-order finite difference scheme for the steady incompressible Navier–Stokes equations, *Int. J. Numer. Methods Fluids*, 20 (1995) 1137–1151.
- [34] J.W. Stephenson, Single cell discretizations of order two and four for biharmonic problems, *J. Comput. Phys.*, 55 (1984) 65–80.
- [35] I. Altas, J. Dym, M.M. Gupta, R. Manohar, Multigrid solution of automatically generated high-order discretizations for the biharmonic equation, *SIAM J. Sci. Comput.*, 19 (1998) 1575–1585.
- [36] C. Clavero, J.L. Gracia, A higher order uniformly convergent method with Richardson extrapolation in time for singularly perturbed reaction-diffusion parabolic problems, *J. Comput. Appl. Math.*, 252 (2013) 75–85.
- [37] A.C. Radhakrishna Pillai, Fourth-order exponential finite difference methods for boundary value problems of convective diffusion type, *Int. J. Numer. Methods Fluids*, 37 (2001) 87–106.
- [38] Z.F. Tian, S.Q. Dai, High-order compact exponential finite difference methods for convection-diffusion type problems, *J. Comput. Phys.*, 220 (2007) 952–974.
- [39] Y. Wang, J. Zhang, Sixth order compact scheme combined with multigrid method and extrapolation technique for 2D Poisson equation, *J. Comput. Phys.*, 228 (2009) 137–146.
- [40] J. Li, Z. Sun, X. Zhao, A three level linearized compact difference scheme for the Cahn–Hilliard equation. *Sci. China-Math.*, 55 (2012) 805–826.
- [41] D.J. Eyre, An unconditionally stable one-step scheme for gradient systems, Preprint. Available from: <http://www.math.utah.edu/~eyre/research/methods/stable.ps>.
- [42] R.J. LeVeque, “Finite difference methods for differential equations”, Lecture notes, University of Washington, 1998.
- [43] J. Shin, D. Lee, S. Kim, J. Kim, A parallel multigrid method for the Cahn–Hilliard equation, *Comput. Mater. Sci.*, 71 (2013) 89–96.
- [44] Message Passing Interface Forum, MPI, A Message Passing Interface Standard, 1994.



- 
- [45] A.S. Almgren, J.B. Bell, P. Colella, L.H. Howell, M.L. Welcome, A conservative adaptive projection method for the variable density incompressible Navier–Stokes equations, *J. Comput. Phys.*, 142 (1998) 1–46.
- [46] M. Sussman, A.S. Almgren, J.B. Bell, P. Colella, L.H. Howell, M.L. Welcome, An adaptive level set approach for incompressible two-phase flows, *J. Comput. Phys.*, 148 (1999) 81–124.
- [47] Y. Li, J. Kim, Phase-field simulations of crystal growth with adaptive mesh refinement, *Int. J. Heat Mass Transf.*, 55 (2012) 7926–7932.
- [48] J. Kim, H. Bae, An unconditionally gradient stable adaptive mesh refinement for Cahn–Hilliard equation, *J. Korean Phys. Soc.*, 53 (2008) 672–679.
- [49] J. Kim, Phase-field models for multi-component fluid flows, *Commun. Comput. Phys.*, 12 (2012) 613–661.
- [50] S. Wise, J. Kim, J. Lowengrub, Solving the regularized, strongly anisotropic Cahn–Hilliard equation by an adaptive nonlinear multigrid method, *J. Comput. Phys.*, 226 (2007) 414–446.

